Critical analysis of strain measurement approaches in tensile testing of nitinol

Valentina Pinto[1,2], Sofia Di Leonardo[1,2], Giuseppe Pitarresi[2], Gaetano Burriesci[1,2,3]*

[1] Fondazione Ri.MED, Palermo, Italy; [2] Engineering Department, University of Palermo, Italy; [3] UCL Mechanical Engineering, University College London, London, UK

* Corresponding author. E-mail address: gaetano.burriesci@unipa.it

Abstract

Nitinol superelasticity is a crucial property for collapsible/expandable cardiovascular implants. The high class of risk associated with these devices requires an accurate mechanical characterisation as starting point for a reliable design methodology. Actual standards (ASTM-F2516) are based on standard metal testing and recommend the use of extensometers for the measurement of average nominal strains during tensile tests.

However, measurement provided by classic extensometers may not be adequate to capture the strain evolution during the material phase transformation. These limitations can be overcome by full-field optical techniques such as Digital Image Correlation (DIC).

This work presents a comprehensive comparison of various techniques for measuring strain on nitinol specimens. These include crosshead position, single and averaging (applied on both sides of the specimen) measurements using physical extensometers, virtual extensometer and 1D and 2D DIC. Results are compared on the basis of the values determined for the upper/lower plateau stress, as defined by ASTM-F2516.

Results shows that the extensometers use on nitinol strips subjected to tensile testing is inaccurate during phase transformation. Physical extensometers also introduce spurious local concentrated pressures at the knives contact region, which may alter the material stress plateaus values. DIC resulted more adequate to provide an accurate evaluation of strain localisation.

Keywords: Nitinol; Shape memory alloy; Superelasticity; Strain measurement; Extensometer; Digital Image Correlation.

1. Introduction

Nitinol is a near-equiatomic Ni-Ti alloy, characterised by the ability to recover levels of strain orders of magnitude larger than standard metals. This unusual behaviour, known as "superelasticity", is accomplished by the onset of regions with different crystal structures and mechanical properties (1,2). These are the result of a stress-induced phase transformation between a parent phase, generally austenite, and a daughter phase, martensite.

In tension, the stress-induced transformation of superelastic nitinol is a highly localised phenomenon occurring across multiple scales, featured by the presence of Lüders-like deformation bands (3–6). The transformation from the parent austenitic phase to martensite initiates at localised regions, often at individual grain boundaries or defects (7,8). As the transformation progresses, these bands propagate through the material, leading to a heterogeneous distribution of strain and, therefore, to the localisation of deformation (9–11)

Nucleation bands form in weak zones characterised by the presence of micro-defects (12), or in regions of stress concentration such as holes and notches (13,14). Furthermore, these are significantly dependant on a number of factors, including the loading rate (15–18), the test temperature (19–21), the number of cycles (22–26) and the geometry (27).

Nitinol superelastic behaviour, coupled with its excellent biocompatibility, makes it the material of choice for several high-risk medical devices, such as stents, stent grafts and transcatheter heart valves (1,28). The criticality of these applications, which demands the highest level of safety, requires an accurate characterisation of the material mechanical behaviour. This is an essential prerequisite to define reliable constitutive models to be used in modern design approaches (29).

The material mechanical parameters are typically obtained from standard tension testing, as outlined in the ASTM E8 (2010) *Tension Testing of Metallic Materials* (30), integrated by the ASTM F2516 (2015) *Nitinol Tension Testing* (31). While the guidelines in these standards recommend the use of physical extensometers for strain measurement, the validity of this method has been questioned, particularly for materials like nitinol that exhibit significant strain localisation (32–34). In fact, as these instruments provide a strain value averaged over the gauge length spanned by the transducer knives, their ability to adequately capture and interpret the material mechanical characteristics is limited, potentially leading to inaccurate representations of the stress-strain behaviour.

Modern optical strain measurement techniques, such as DIC, overcome the limitations of traditional methods by enabling non-contact, full-field detection of the strain distribution across the specimen. As a result, DIC has become a key tool for analysing the global and local mechanical behaviour of nitinol, and is now widely used to investigate its complex thermo-mechanical response (6,13,14,16,18,21,25–27,35–40). DIC has provided direct visualisation of the highly localised deformation and of the nucleation, propagation and regression of transformation bands during superelastic loading cycles (26). It has also contributed to clarify the role of intersecting phase transformation fronts in relaxing in-plane bending moments (41), and has been employed to analyse the geometric influences on strain localisation, showing that the specimen aspect ratio governs the number and morphology of transformation bands (27,42,43). Furthermore, DIC has contributed to understanding fatigue mechanisms, demonstrating that cracks frequently initiate the transition zone between austenite and martensite (6,38,44). The rate-dependent nature of phase transformation and stress hysteresis has been systematically analysed using DIC (17,45), and combined DIC/infrared measurements have been used to investigate thermo-mechanical coupling at different loading rates (15). Additional work has explored localised temperature–strain coupling, and the strain memory retained by martensite during cyclic loading (36).

This work presents a critical analysis of the most common strain measurement approaches applied in tensile testing of nitinol, with the aim to identify the strength and limitation of the different methods. Strain evaluated from crosshead position, single and averaged measurements employing physical extensometers, virtual extensometers, and 1D and 2D DIC were evaluated. Comparison focuses on the accuracy and reproducibility in the measurement of the material parameters defined for nitinol mechanical characterisation in the ASTM F2516 (31), taking as a gold standard the measurement methodology described in (40).

The study provides a comprehensive evaluation of each technique, outlining their strengths and limitations for specific purposes and guiding a more informed decision in tests setup.

2. Materials and methods

2.1. Sample preparation

Three test specimens, 100.0 mm long, 10.0 mm wide and 0.4 mm thick, were obtained from the same nitinol plate (56% Ni, 44% Ti).

To determine the phase composition at test temperature, a 38.6 mg sample from the plate was analysed by differential scanning calorimetry (DSC). A sequence of cooling and heating ramps was applied in the range from -40 °C to 200 °C at a constant rate of 5 °C/min. The heat flow was obtained as a function of the temperature (reported in Figure 1), allowing to identify the phase transformation temperatures, as described in the standard ASTM F2004-03 (46). Analysis of the cooling curve indicates that the start, peak and finish phase transformation temperatures were M_s = 3.3 °C, M_p = -4.1 °C and M_f = -16.4 °C, respectively. From the heating curve, the austenitic start, peak and finish phase transformation temperatures were A_s = -8.5 °C, A_p = -1.6 °C and A_f = 5.1 °C, respectively. These temperatures confirm that the material is fully austenitic at room temperature and exhibits superelastic behaviour during testing, in accordance with ASTM F2516 (31).

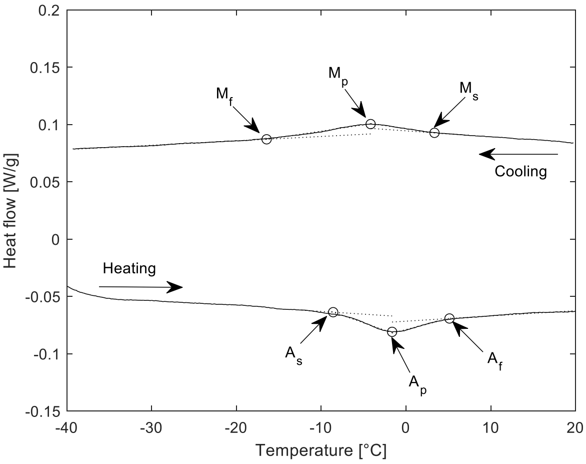

Figure 1. DSC heat flow curve.

The strips were cut via electrical discharge machining, in order to minimise the formation of residual stresses and heat affected zones at the cutting regions.

To provide texture for DIC measurements, one of the surfaces in each specimen was prepared applying a uniform matte white base coat with an airbrush, followed by randomly distributed matte black speckles.

2.2. Plan of experiments

A sequence of tensile tests was performed on each sample. Each tensile test was conducted under identical conditions on an Instron 3367 uniaxial electromechanical testing machine (Instron, Norwood, MA, USA) at room temperature, in displacement control, applying a quasi-static triangular load. In particular, load was increased from zero to 2300 N, ensuring that the sample achieved a stress-induced martensitic transformation over the whole visible area of the specimen, and then unloaded to zero force. Loading and unloading ramps were performed at a constant crosshead velocity of 1 mm/min.

For each specimen, the first test (Test 1) was performed using only digital image correlation (DIC) to capture the undisturbed strain-field evolution, providing a baseline reference. The second test (Test 2) combined DIC with measurements from two physical extensometers mounted on opposite sides of the specimen. This configuration enabled simultaneous comparison of the techniques and assessment of any influence exerted by the extensometers on the material response. Finally, a third test (Test 3) was carried out after removing the extensometers, again using DIC alone, to verify whether their temporary application had introduced any local effects or modifications in the strain behaviour. No manipulation of the specimen occurred between the tests other than the mounting and removal of the extensometers.

For each test and for each measurement method, engineering stress versus strain curves were evaluated during the whole cycles. Engineering stress was calculated as the ratio of the force measured by the load cell to the initial cross section. As described in the ASTM F2516 (31), stress-strain curves were processed to calculate the reference parameters for nitinol characterisation:

- upper plateau stress (UPS): stress measured at 3% of strain during loading;
- lower plateau stress (LPS): stress measured at 2.5% of strain during unloading.

These parameters were obtained from the different strain measurement methods and used for comparison. Figure 2 describes the experimental setup and shows the position of the physical extensometers, the different regions analysed with DIC, and the reference used for the virtual extensometer.

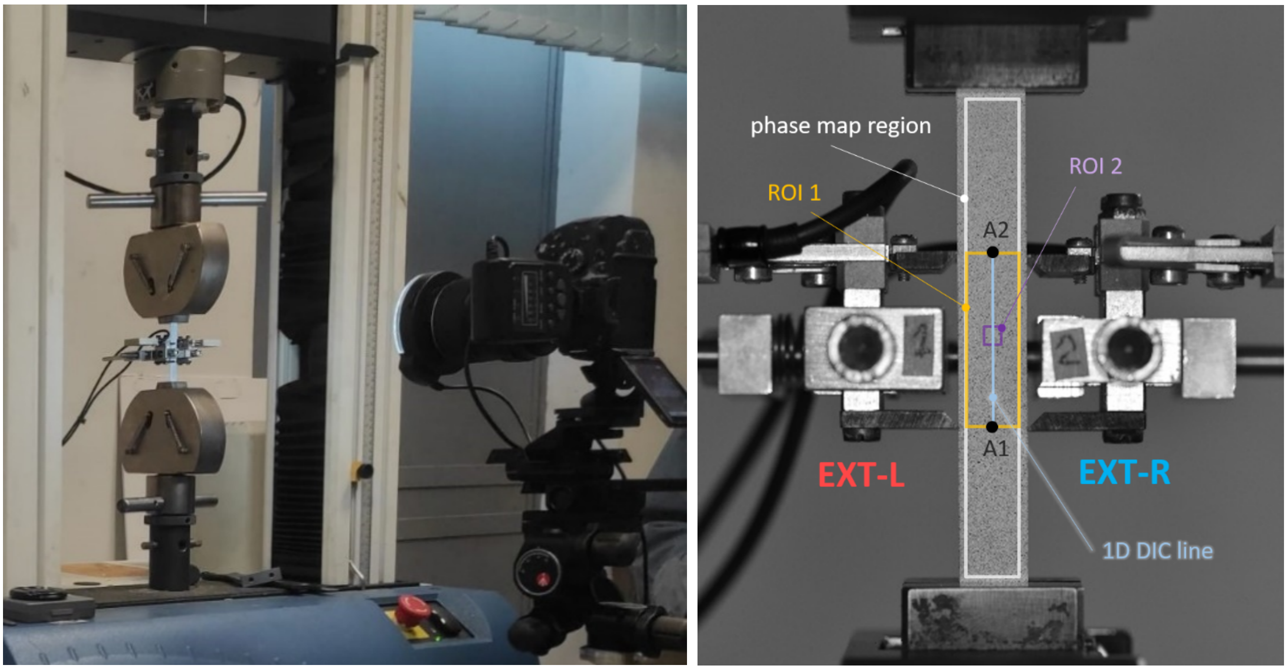

(a) (b)

Figure 2 (a) experimental setup and (b) representation of: physical extensometer (EXT-L and EXT-R); virtual extensometer points (A1-A2) in black; 1D DIC line in light blue; phase map region in white; ROI 1 in yellow and ROI 2 in purple.

2.3. Crosshead strain

Crosshead strain was obtained for each test as the ratio between the crosshead displacement measured by the testing machine and the initial gauge length, whose measure was equal to 77.5 mm.

2.4. Physical extensometer

Two HBM DD1 extensometers (Hottinger Baldwin Messtechnik GmbH, Wien, Austria) were used in Test 2 and mounted in an averaging axial setup, with each transducer on an opposite side of the specimen (EXT-L on the left and EXT-R on the right), through a DD1/ZE quick clamp kit (see Figure 2b). The extensometers knives were positioned to define a nominal gauge length of 25 mm on both sides, with each extensometer connected to an independent Wheatstone-bridge channel. This setup enables simultaneous, independent strain measurements on both sides of the specimen, allowing the detection of spurious flexural effects. The instantaneous average of the two strain measurements provided by EXT-R and EXT-L, here abbreviated as EXT-AVG, was calculated at each point in time for all tests.

The two extensometers were monitored on a D4 Wheatstone bridge from Vishay Micro-Measurements (Toronto, Canada), allowing a sampling rate of 8 Hz. A calibration rod was used to determine the initial gauge length and verify the nominal sensitivity of the gauges (1 mV/V×mm).

2.5. Virtual extensometer

Virtual extensometer strain was calculated tracking the relative displacement of two reference points selected on the specimen axis, covering the same gauge length of the physical extensometer (A1 and A2 in Figure 2b) (47,48). Being this measurement line close to the neutral axis of the specimen, it is characterised by a stress level about correspondent to the stress estimated from the loadcell (40). Hence, the relationship between the local stress and the local strain is less affected by the spurious bending moment caused by the inhomogeneous behaviour of the material. The two reference points were selected at the same axial position where the extensometers knives in Test 2 contact the specimen sides. This approach essentially mimics the physical extensometer concept, but avoiding the presence of the mechanical contact forces on the specimen. This allows to identify and analyse the alterations introduced by the presence of the physical extensometers.

2.6. Digital image correlation analysis

DIC analysis was performed during all tests, by monitoring the deformation of the speckle applied on the specimen surface through image processing algorithms. DIC is an optical technique for the measurement of full-field displacements and strains distribution, based on the comparison of digital images of a component acquired at different loading stages (49). The speckle pattern was applied to ensure a random, isotropic distribution with high contrast between the speckles and the background, aiming for an ideal surface-to-speckle coverage ratio of 50:50. Acquisitions were taken at 0.2 Hz, using a digital reflex Nikon D5100 camera (Nikon Corporation, Tokyo, Japan), equipped with a macro lens AF-S VR Micro-Nikkor 105 mm f/2.8G IF-ED (Nikon Corporation, Tokyo, Japan). The camera was placed on a tripod with a 4-ways rail slider for fine focus, and was operated remotely with the open-source software 'digiCamControl'. A LED macro ring light was mounted on the camera lens, to provide an optimal shadow-less illumination of the sample.

The open-source 2D DIC program Ncorr, operated in Matlab (MathWorks, Massachusetts USA), was used to correlate the acquired images (50). The tracking is obtained by looking for a subset in the deformed image, called test subset, which has the distribution of light intensity closer to that of the subset in the undeformed image (called reference subset) within the region of interest (ROI). Displacement and strain maps were obtained by setting a millimetre to pixel ratio of 0.017 mm/px, subset radius of 15 px, a subset spacing equal to 50 % of the subset radius, and a virtual strain gauge of 3 subset spacings. The resulting maps were then post-processed in Matlab.

DIC analysis was initially applied to one dimension (1D DIC) (11), covering the same gauge length as the physical and virtual extensometers (A1 and A2 in Figure 2b) along the specimen axis, where the effect of lateral compression of the extensometer knives and the spurious bending moment caused by the inhomogeneous behaviour of the material are less influent.

2D DIC analysis was then performed on the ROI indicated as 'phase map region' in Figure 2b (white rectangle). The horizontal dimension of this area was taken slightly smaller than the physical sample boundaries, to avoid edge errors typically introduced when a deformed subset includes part of the background field of view (51).

Full field strain maps were obtained from the phase map region as described in (40). Maps are reported for the nine selected configurations of the testing cycle indicated in Figure 3:

- Configuration 1: halfway between the upper and lower plateau, in the austenitic loading phase;
- Configuration 2: along the upper plateau, at 10 % of the strain associated with the austenite to martensite transformation;
- Configuration 3: along the upper plateau, at 50 % of the strain associated with the austenite to martensite transformation;
- Configuration 4: along the upper plateau, at 90 % of the strain associated with the austenite to martensite transformation;
- Configuration 5: in the martensitic unloading phase, halfway between the upper and lower plateau;
- Configuration 6: along the lower plateau, at 90 % of the strain associated with the martensite to austenite transformation;

- Configuration 7: along the lower plateau, at 50 % of the strain associated with the martensite to austenite transformation;
- Configuration 8: along the lower plateau, at 10 % of the strain associated with the martensite to austenite transformation.
- Configuration 9: halfway along the unloading fully austenitic phase down to zero.

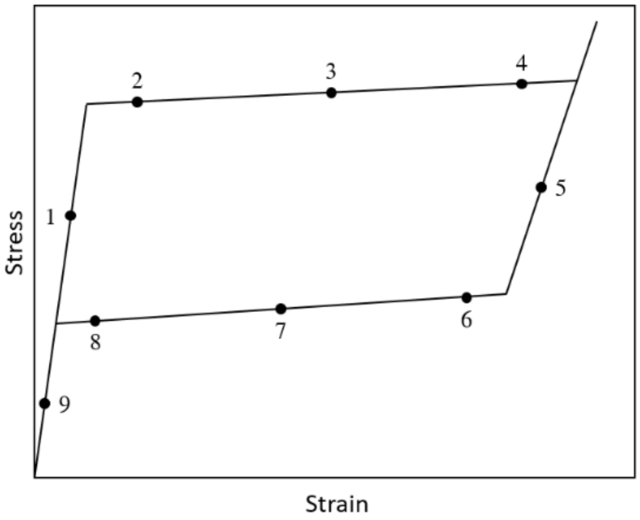

Figure 3. Schematic representation of the stress versus strain curve with the selected configurations of the amplified strain maps.

DIC mean strain values were obtained averaging the strain over two further ROIs of different dimensions: a rectangular region with height equal to 25 mm, covering the length between the extensometers knives (ROI 1, yellow rectangle in Figure 2b); and a square region covering 25 % of the specimen width and centred at the geometric axis of the specimen (ROI 2, purple square in Figure 2b). The choice of size and position of ROI 2 is based on a previous work (40), where five square ROIs of identical dimensions were analysed at different axial locations along the specimen, from the central region up to a distance from the grips equal to the specimen width. The coexistence of austenite and martensite with substantially different Young's moduli in the cross sections interested by the transformation front induces a local shift of the neutral axis. When the ROI becomes too small, this eccentricity introduces larger deviations between the local and nominal axial stress. The 25% specimen-width ROI was shown to minimise this effect, while smaller ROIs tend to introduce larger deviations from the nominal stress and would require a finer speckle pattern, incompatible with the DIC resolution needed for the full-field analyses conducted across all tests. Therefore, ROI 2 represents an optimal compromise. Moreover, the resulting estimates of the material parameters showed only minimal variability across ROI locations, indicating that the extracted parameters are robust and only marginally affected by the ROI position. Based on these findings, ROI 2 represents a reliable and validated reference region for quantifying the local strain response associated with phase transformation.

3. Results

Strain localisation patterns over time at the specimen axis, evaluated through 1D DIC, are reported in Figure 4 for each test. 1D DIC offers the advantage to capture the localised effects associated with the phase transformation, such as the propagation and regression of martensitic transformation in time (reported in Figure 4).

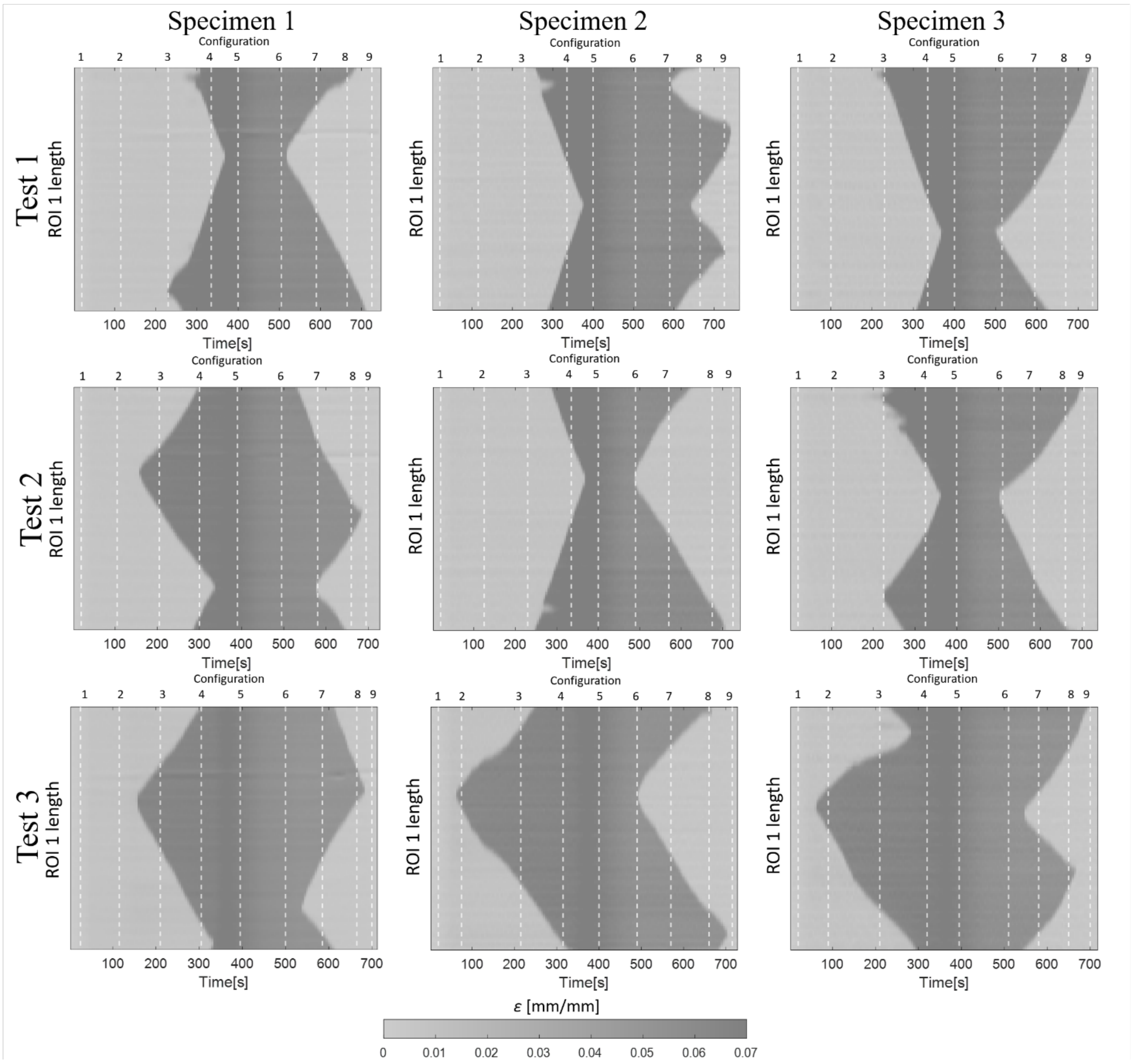

Figure 4. Strain localisation patterns over time evaluated by 1D DIC.

The results from the DIC analysis conducted on the phase map region (white rectangle in Figure 2b) were postprocessed as described in Figure 5 (40). The strain maps confirm the characteristic bipolar behaviour of nitinol: martensitic regions (red regions in the strain map) exhibit about uniformly distributed strains around 0.07 mm/mm, while austenitic regions (blue regions in the strain map) remain below 0.01 mm/mm. The gradual strain transition between these two regions observed in the non-binarized strain map (green-yellow regions) is an artefact of the DIC method, as this cannot resolve sharp strain discontinuities occurring over dimensions smaller than the subset size. To address this limitation, a threshold-based binarization was adopted. In fact, challenges associated with inadequate spatial resolution of DIC shall be addressed when higher degrees of accuracy are required in the evaluation of phenomena connected with localisation of phase transformation (40). Regions of small axial strains associated with the austenitic phase ($\varepsilon < 0.035$ mm/mm) are represented in light grey, and regions of large axial strain associated with the martensitic phase ($\varepsilon > 0.035$ mm/mm) are represented in dark grey. The threshold strain value of 0.035 mm/mm was chosen as approximately 50% of axial transformation strain associated with the austenite to martensite transformation. To enhance visualisation of the lateral displacement, the original strain maps have been distorted by applying the local displacement vectors obtained from the DIC analysis to each pixel, amplifying the normal component of one order of magnitude (see right panel in Figure 5). Horizontal displacements were amplified by a factor of 10, while the vertical scale was maintained. This amplification allows for a clearer representation of the bending behaviour. Moreover, in each strain maps, ROI 1 and ROI 2 borders are indicated in black and in white, respectively. The axial line on which the virtual extensometer points were selected and 1D DIC were evaluated is represented in black.

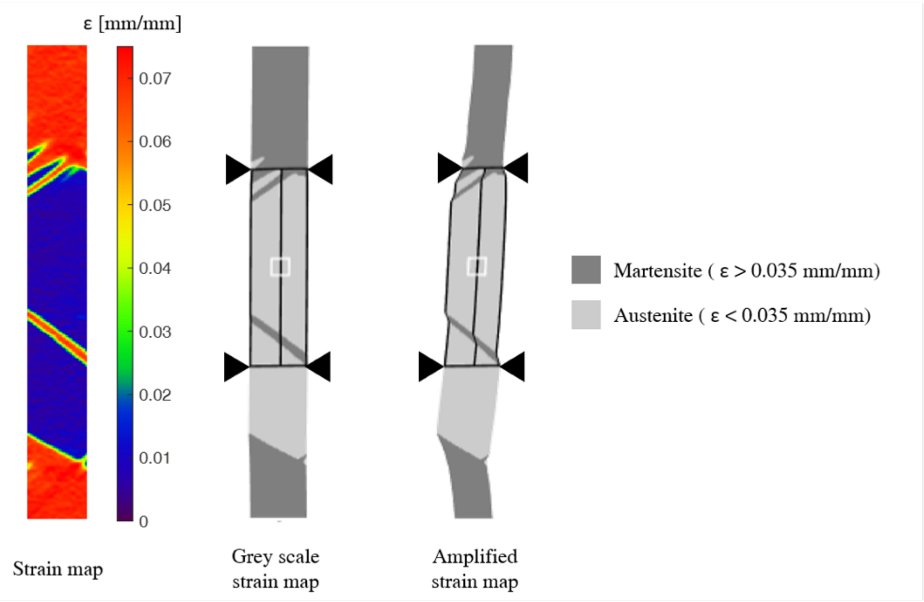

Figure 5. DIC strain map (left), corresponding binarized map (grey scale strain map in the centre), and binarized strain map with horizontal displacement field amplified by a factor of 10 (amplified strain map in the right).

The results for the three specimens are summarised in Figure 6-Figure 8, including the stress versus strain curves and the full field deformation maps at the nine selected configurations.

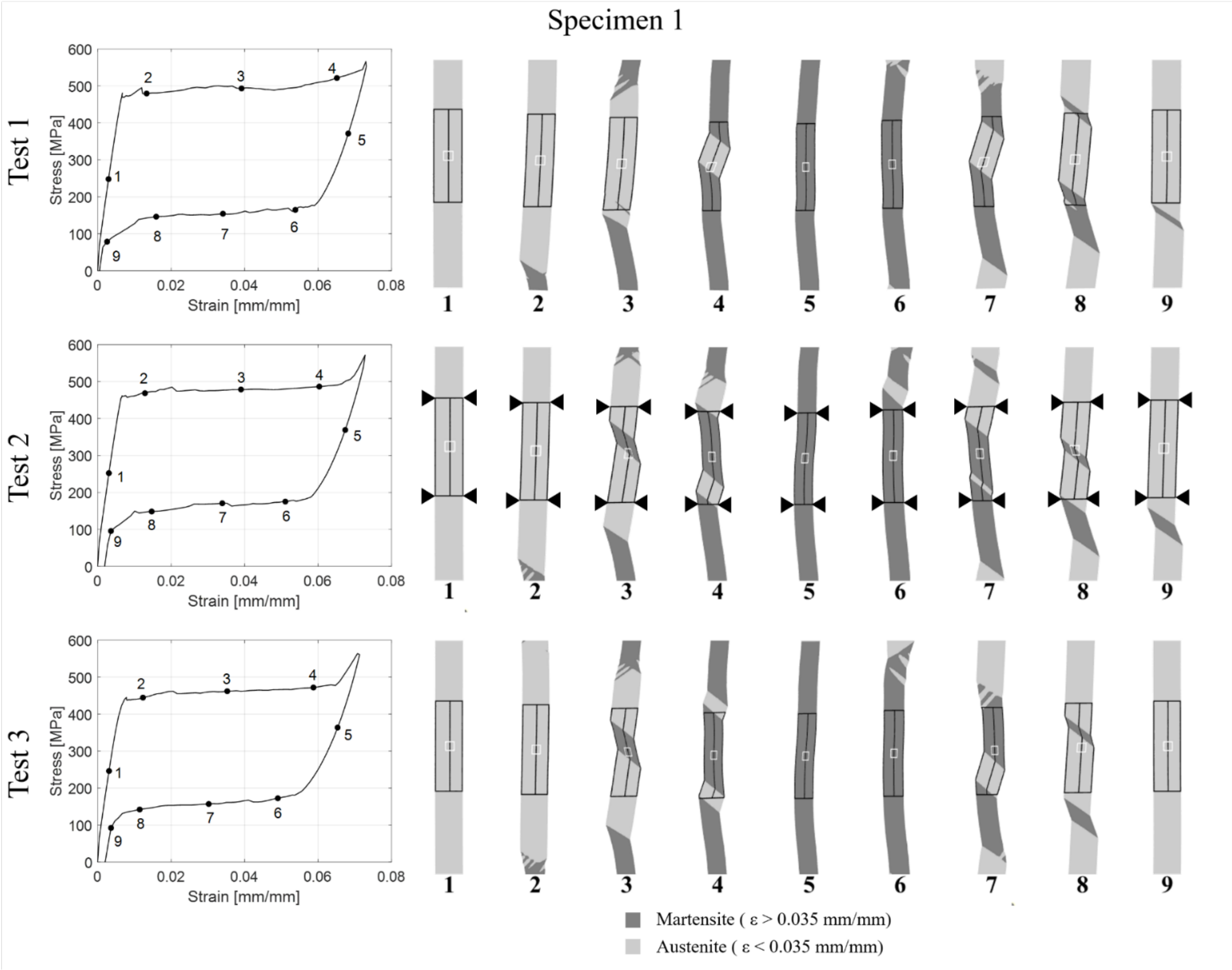

Figure 6. Stress versus strain curves and strain maps at 1-9 configurations for specimen 1. Strain reported in the curves and strain maps were calculated using the phase map region. Physical extensometers are represented in test 2 by means of black triangles. ROI 1 and ROI 2 borders are represented in black and white, respectively. Line on which virtual extensometer points are selected and 1D DIC are evaluated is indicated in black.

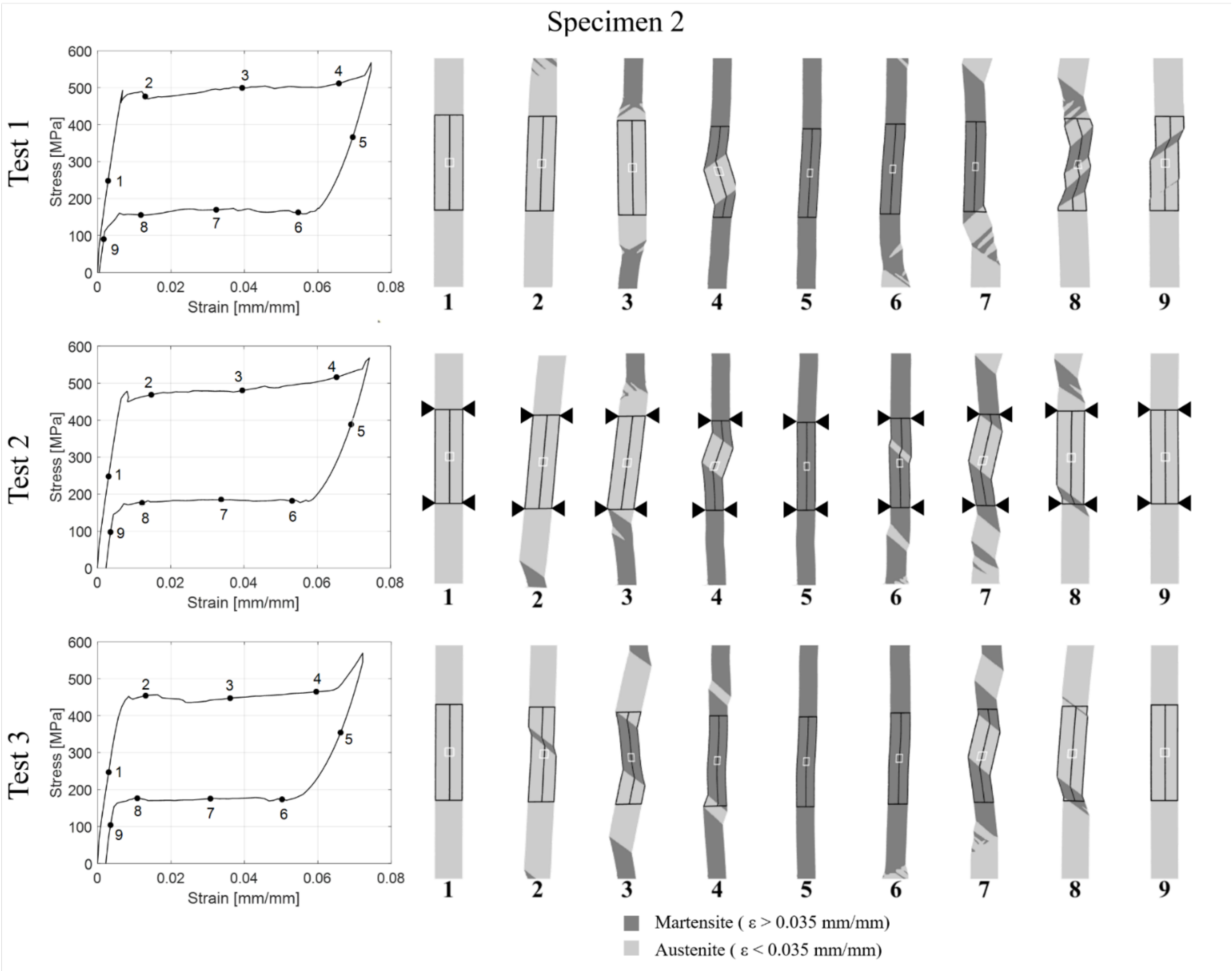

Figure 7.Stress versus strain curves and strain maps at 1-9 configurations for specimen 2. Strain reported in the curves and strain maps were calculated using the phase map region. Physical extensometers are represented in test 2 by means of black triangles. ROI 1 and ROI 2 borders are represented in black and white, respectively. Line on which virtual extensometer points are selected and 1D DIC are evaluated is indicated in black.

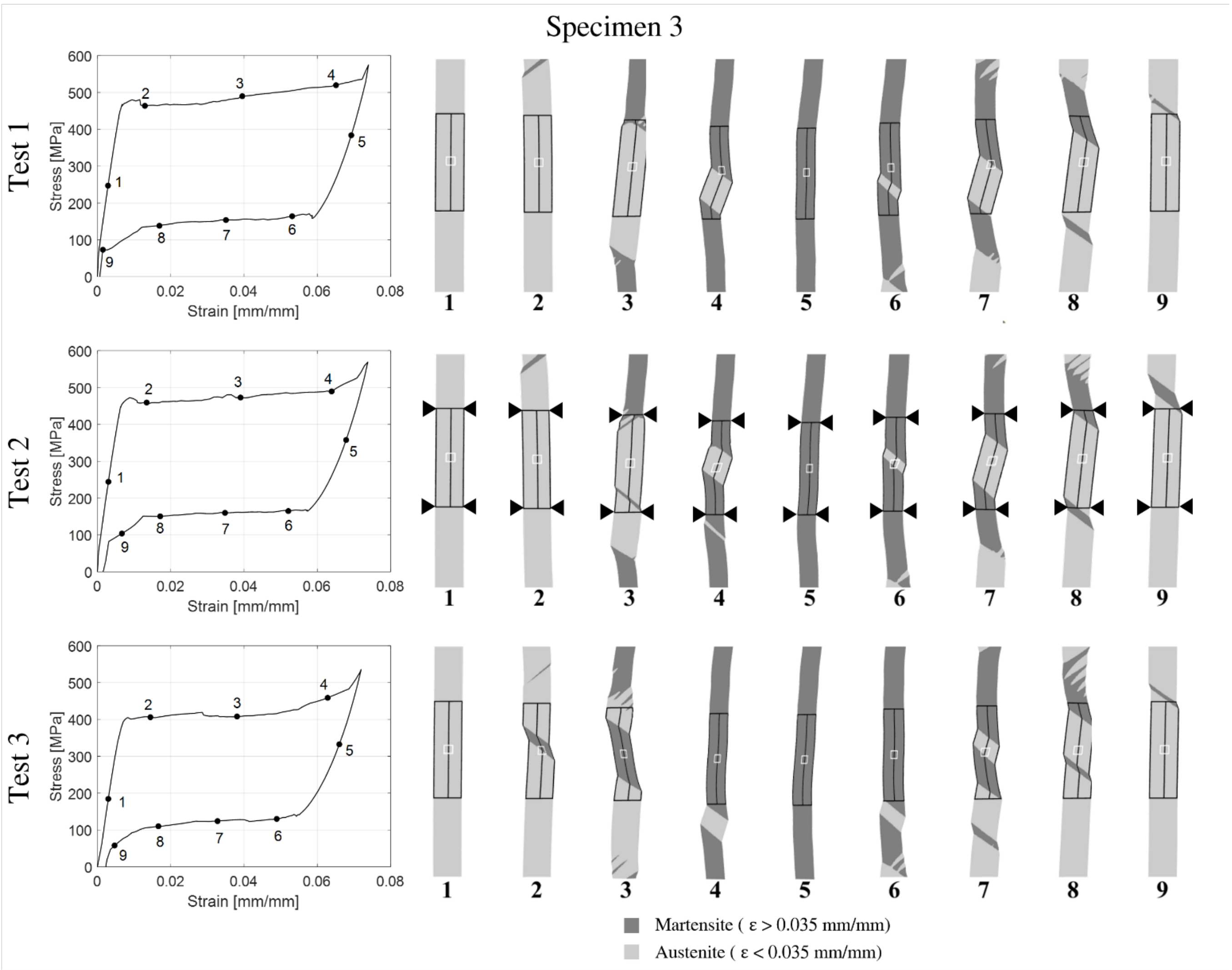

Figure 8. Stress versus strain curves and strain maps at 1-9 configurations for specimen 3. Strain reported in the curves and amplified strain maps were calculated using the phase map region. Physical extensometers are represented in test 2 by means of black triangles. ROI 1 and ROI 2 borders are represented in black and white, respectively. Line on which virtual extensometer points are selected and 1D DIC are evaluated is indicated in black.

In Test 1, the strain maps sequence reveals a progressive phase transformation process. The initiation point for this transformation is observed at the gripped regions (see configurations 2-3 in Figure 6-Figure 8). From these points, the transformation propagates along the gauge length, gradually moving towards the central regions (configurations 3-5 in Figure 6-Figure 8). This behaviour is a typical characteristic of straight nitinol specimens subjected to tensile loading, associated with the presence of stress concentrations introduced by the grips clamping action (52). During the unloading phase, the transformation follows a reverse path: the phase transformation reverts from the central region towards the gripped regions (configurations 6-9 in Figure 6-Figure 8), indicating a reversible nature of the phenomenon under the applied loading conditions. The amplification of the horizontal displacements highlights the distortions that the specimen experiences to accommodate the uneven vertical elongations induced by the propagation of oblique phase transformation fronts. This necessarily results into the presence of a spurious bending moment (40).

Test 2 shows a spurious effect deriving from the presence of the physical extensometers, which appear to alter the propagation of the transformation, moving the propagation fronts towards the region encompassed by the knives. The effect of the extensometers is especially evident in the deformation maps obtained for specimen 3, where additional Lüders bands appear to originate from the sites where the extensometers knives contact the specimen (see configuration 3 in Figure 8). This behaviour is likely related to the local compression produced by the knives, which can increase the local effective stress and promotes the initiation of phase transformation. A similar effect is observed in specimen 1 and 2, especially during reverse transformation: the last regions to return to austenite are those located near the extensometer knives (configurations 8-9 in Figure 7 and Figure 8). These effects appear to introduce irreversible changes in the transformation pattern, as they partially re-emerge in Test 3, after removal of the extensometers.

Extensometers nominal strain versus time curves, obtained from Test 2 for each specimen, are reported in Figure 10. Diagrams show an initial strain increase relative to the homogeneous austenite elastic deformation, which suddenly plateaus as the material develops the first Lüders transformation band. The deformation, then, starts increasing again only after a transformation front enters the extensometers gauge area. As the transformation propagates within the gauge region, the strains measured on the right and left sides progress at different rates. A substantial difference between EXT-R and EXT-L is observed for specimens 1 and 2 between configurations 6 and 9, as the propagation of the phase transformation fronts produces different axial elongations along the left and right sides of the specimen within the extensometer gauge region (see Figure 6 and Figure 7). In fact, significant differences between the elongations measured on the right and left specimen edges (EXT-R and EXT-L) arise when the phase distribution within the extensometer gauge region becomes asymmetric, as shown in Figure 9-A.

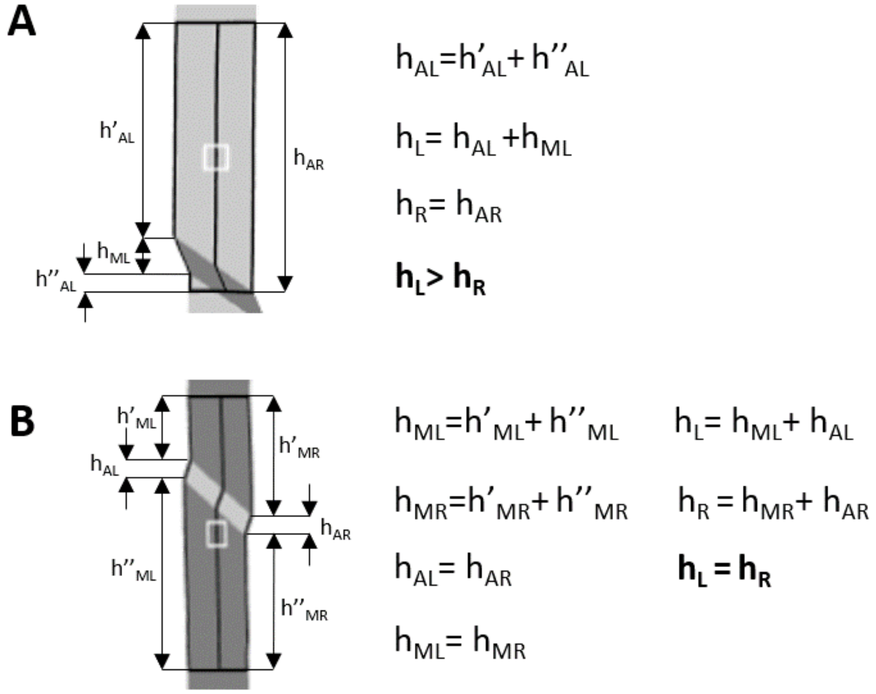

Figure 9. Schematic illustration of phase distribution within the extensometer gauge region: (A) asymmetric configuration leading to different elongations measured on the left and right edges; (B) symmetric configuration with equal phase fractions on both specimen edges.

Since the strain levels within the martensitic and austenitic regions are approximately uniform, such asymmetry emerges when the cumulated axial lengths occupied by each phase along the left (h_{ML}, h_{AL}) and right edges (h_{MR}, h_{AR}) within the extensometer gauge region differ. This condition typically occurs when the transformation front enters or exits the gauge area, producing a mismatch in the proportions of austenitic and martensitic material measured by each extensometer ($h_L > h_R$ or $h_R > h_L$). please note that, in some configurations (Figure 9-B) the axial gauge lengths occupied by the martensitic and austenitic phases (h_M and h_A, respectively) are essentially identical on both sides of the specimen despite the presence of transformation fronts within the gauge length. Since, as observed above, the strain within each phase is nearly uniform, the resulting axial elongation measured by EXT-R and EXT-L remains similar, even in the presence of bending. Interestingly, when the whole specimen is in the martensitic state, the curves measured on the two sides maintain slightly different values, indicating the presence of residual bends in the specimen, also observed in configurations 5 of Figure 6-Figure 8. This indicates that averaging extensometers setups are preferable to the standard single extensometer solution recommended by the relevant ASTM standards. In fact, the average value of the measurements determined on the two sides (see black line in Figure 10) can minimise the effect of spurious bending loads and better represent the global strain state of the specimen.

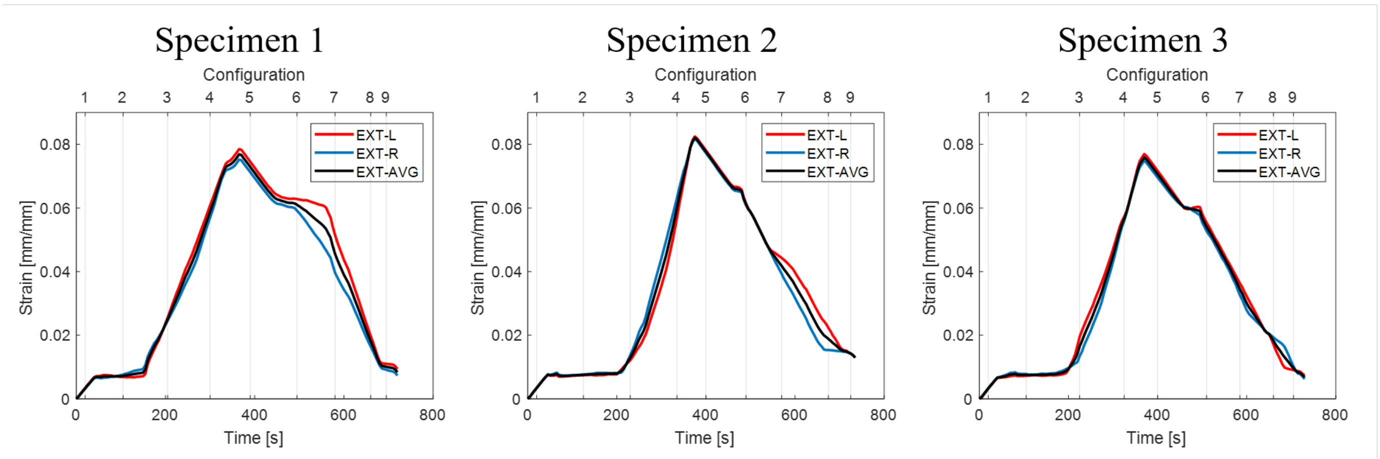

Figure 10. Strain versus time curves associated with left (EXT-L), right (EXT-R) and average (EXT-AVG) extensometers for specimen 1, 2 and 3, respectively.

Figure 11 reports a comparison between the strains estimated with crosshead displacement, 1D DIC, 2D DIC averaged over ROI 1 and ROI 2 (see Figure 2b), and the strain calculated from the virtual extensometers (see Section 2.5), for each test. To better identify ROI windows in each strain configuration in Figure 6-Figure 8, borders of each ROI are represented on the strain maps.

The diagram illustrates that strain measurements based on crosshead position provide limited accuracy compared to more sophisticated techniques. In fact, this approach fails to capture the localised phase transformations, resulting in a simplified triangular strain profile that does not capture the complex deformation behaviour observed in the material. Moreover, strain measurements based on crosshead displacement tend to overestimate the actual axial strain, owing to uncertainty in the effective gauge length, friction-induced sliding at the grips, and localised grip-affected deformation. As a result, the maximum strain measured from the crosshead (~0.08 mm/mm) consistently exceeds that obtained from the optical methods (~0.07 mm/mm). The relative impact of gauge-length uncertainty typically decreases for slender specimens with larger axial dimensions, improving the reliability of crosshead-based estimates in those cases.

It is evident from the diagrams that the 1D DIC, ROI 1 and axial virtual extensometer curves exhibit a similar trend. This is expected, as all these approaches are applied to the same axial length (as the physical extensometer).

Curves associated with ROI 2 exhibit abrupt changes in deformation when a transformation front reaches the analysed region (e.g., configuration 4 of Test 1 of specimen 1 in Figure 11). When the front originates outside the ROI, the response is preceded by a plateau, reflecting the progression of the transformation in regions not included in the ROI. Conversely, when the transformation nucleates directly within the ROI, no plateau develops: the onset of the transformation immediately produces a sudden increase in the measured deformation, as observed in Test 3 of specimens 2 and 3. These curves better highlight the local phase transformation from austenite to martensite, and are therefore more independent on the test setup, resulting more representative of the material behaviour.

The width of the bell shape described by the curves appears to substantially reduce from Test 1 to Test 2, to re-expand to the largest value in Test 3 (with exception of specimen 1, that shows a consistent expansion in the bell shape at each cycle).

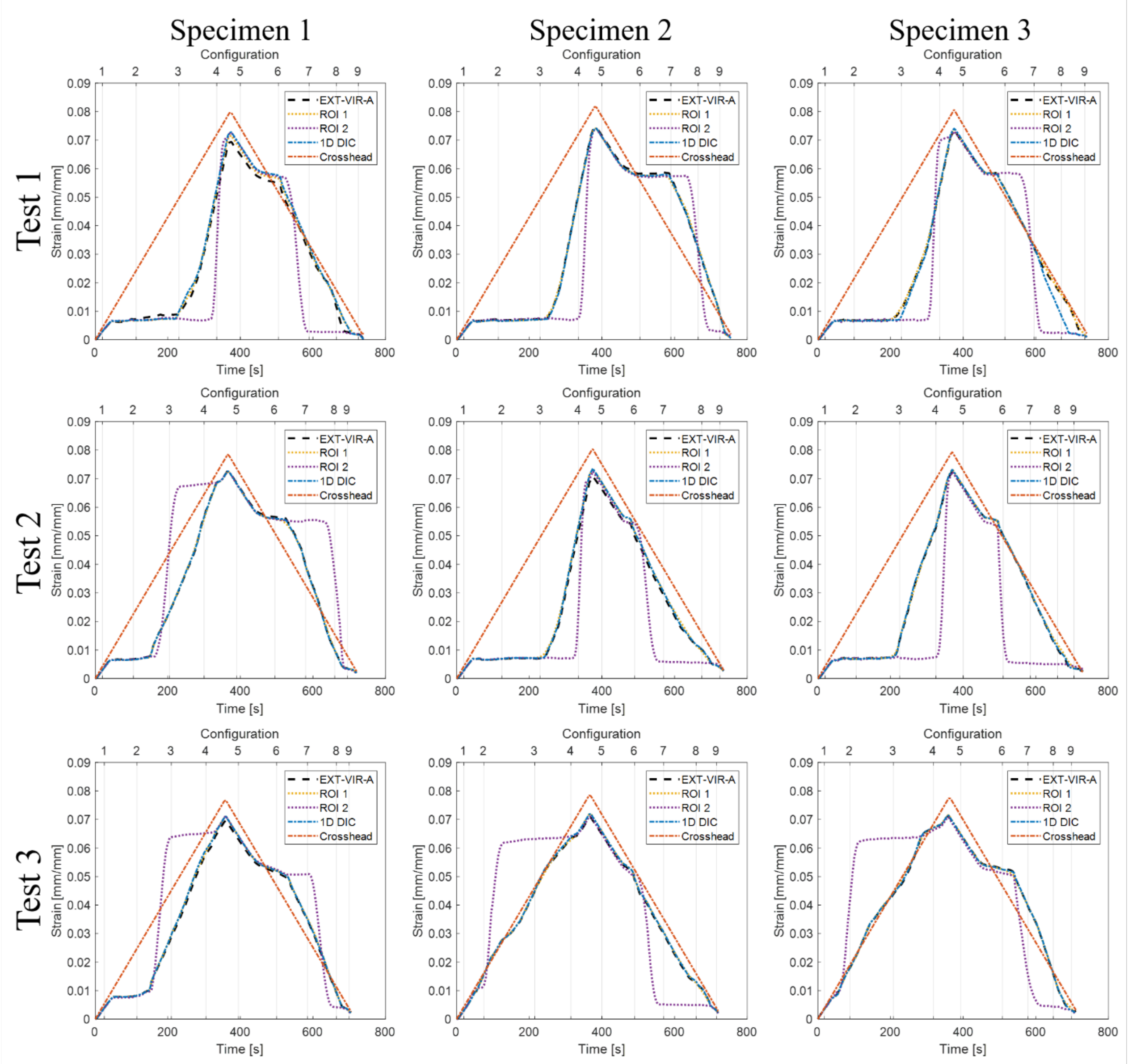

Figure 11. Strain versus time curves considering for each test the strain measured by the axial virtual extensometer (dashed black curves), average strain on ROI 1 (dotted yellow curves) and ROI 2 (dotted purple curves), and the strain measured by 1D DIC (dash-dot blue curves) and crosshead position (dash-dot orange curve).

The values of the stress mechanical parameters, UPS and LPS, obtained with the different approaches, are summarised in Table 1.

Table 1. Nitinol stress mechanical parameters obtained by means of each strain measurement method, with respective percentage deviation compared to the reference ROI 2 in brackets.

PARAMETER [MPa]	**Specimen 1**			**Specimen 2**			**Specimen 3**		
	Test 1	**Test 2**	**Test 3**	**Test 1**	**Test 2**	**Test 3**	**Test 1**	**Test 2**	**Test 3**
UPS - Crosshead	482.58	478.33	461.30	474.98	474.85	435.69	466.22	462.02	451.23
	(7%)	(1%)	(1%)	(9%)	(9%)	(4%)	(9%)	(10%)	(2%)
UPS - EXT L		477.73			494.43			481.21	
		(1%)			(5%)			(7%)	
UPS - EXT R		478.45			487.76			485.75	
		(1%)			(6%)			(6%)	
UPS - EXT AVG		477.88			493.46			482.79	
		(1%)			(5%)			(6%)	
UPS - VIRT EXT	503.22	478.45	462.34	500.80	499.53	435.81	508.53	481.33	449.17
	(3%)	(1%)	(1%)	(4%)	(4%)	(4%)	(1%)	(7%)	(2%)
UPS – 1D DIC	497.90	478.45	462.34	500.80	499.53	435.67	506.65	481.33	449.17
	(4%)	(1%)	(1%)	(4%)	(4%)	(4%)	(1%)	(7%)	(2%)
UPS - ROI 1	497.90	478.45	463.11	500.80	499.53	435.67	506.65	481.33	449.17
	(4%)	(1%)	(2%)	(4%)	(4%)	(4%)	(1%)	(7%)	(2%)
UPS - ROI 2	**521.27**	**475.13**	**456.26**	**519.13**	**519.69**	**456.09**	**513.69**	**515.28**	**440.51**
LPS - Crosshead	151.07	163.60	153.96	170.30	181.18	170.95	149.22	156.80	154.95
	(4%)	(12%)	(1%)	(6%)	(0%)	(3%)	(3%)	(6%)	(3%)
LPS - EXT L		151.17			178.94			156.79	
		(3%)			(1%)			(6%)	
LPS - EXT R		156.48			182.69			158.85	
		(7%)			(1%)			(4%)	
LPS – EXT AVG		152.82			179.78			156.79	
		(5%)			(1%)			(6%)	
LPS – VIRT EXT	151.40	160.50	153.76	156.33	184.49	171.87	149.58	157.59	149.71
	(4%)	(10%)	(0%)	(3%)	(2%)	(3%)	(3%)	(5%)	(7%)
LPS – 1D DIC	151.11	160.50	153.16	156.33	184.76	171.98	149.58	157.59	149.71
	(4%)	(10%)	(0%)	(3%)	(2%)	(3%)	(3%)	(5%)	(7%)
LPS – ROI 1	151.77	160.50	153.16	156.33	184.76	171.98	148.73	157.59	149.71
	(4%)	(10%)	(0%)	(3%)	(2%)	(3%)	(4%)	(5%)	(7%)
LPS – ROI 2	**157.52**	**146.10**	**153.16**	**161.18**	**181.61**	**177.04**	**154.18**	**166.07**	**160.52**

The parameters in Table 1 reveal that UPS has a gradual but significant decrease from Test 1 to Test 2 to Test 3. Instead, LPS generally shows an increase in Test 2, where the extensometers are present, followed by a decrease in Test 3, where the transducers are removed.

Cycling of nitinol is commonly associated with changes in the UPS and LPS values, which progressively tend to reduce. In fact, it is well-established that the material exhibits a mixture of phases at the conclusion of each loading cycle, due to the presence of residual martensite in the unloaded configuration. This phenomenon, that can be attributed to the accumulation of residual strains in the material, causes a progressive reduction in the energy required to reactivate the phase transformations with increasing cycle numbers (17,22,24,25).

It is interesting to observe that, when the physical extensometer is present, this trend is inverted and the LPS value consistently increases from Test 1 to Test 2, recovering the expected tendency once the transducers are removed (in Test 3). This can be justified by the actions associated with the presence of the extensometers. In fact, their knives introduce localised compressive lateral forces, discontinuity in the normal force and an out of plane bending moment, due to the quick clamps and to the additional weight of the system (comprising the extensometers and their holding rig) (34). These actions appear to be able to trigger the onset of new Lüders bands at the knives locations, altering the mechanical response of the specimen.

4. Discussion

Different measurement methods for the determination of strain in tensile testing were applied to superelastic nitinol specimens and compared in terms of performance.

Crosshead strain measurement offers a very simple method for estimating deformation, which requires minimum equipment and processing. However, it provides global average strain results inadequate to capture complex strain localisations typical of nitinol. Moreover, the accuracy of the strain measurements is influenced by factors such as the assumption in the gauge length value (the appropriate value is difficult to estimate due to the inhomogeneous behaviours), friction between the specimen and the grips causing sliding and readjustment during the test, frame stiffness, specimen alignment and the specimen volume affected by the tightening of the grips. These factors become less influent or negligible for highly slender specimens such as long wires, for which the use of the cross-head displacement is, in fact, more appropriate and very common.

Hence, despite crosshead strain measurement being a simple and widely used technique, it may not be suitable for materials that exhibit complex deformation behaviours, especially when high levels of accuracy are required. Specifically, as demonstrated in Table 1, deviations larger than 10 % in the estimation of material parameters (UPS and LPS) were observed in the presented tests, compared to the gold standard 2D DIC measurements on ROI 2. It needs to be said that these approximations are expected to reduce for slender specimens of larger axial lengths.

Physical extensometers provide a direct measurement of the strain between two points of the specimen, bypassing the limitations associated with estimating the gauge length and friction between the specimen and the grips. However, the contact force exerted by the extensometer knives induces additional local stresses which may alter the nucleation and propagation behaviour of martensitic bands. Additionally, these methods are affected by low spatial resolution associated with the distance between the knives. This, in fact, reduces their ability to capture strains during the complex phase transformation process of nitinol, as the transformation front produces significant differences in elongation on opposite sides of the specimen. Hence, extensometer readings can be influenced by the specific location of the measurement.

Using averaging extensometers can partially mitigate this issue, although the presence of additional contact points introduces more stress concentrations, altering further the nucleation and progression of the phase transformation front and the material response. However, for the sole purpose of identifying material parameters, physical extensometers remain a reasonably accurate option, with average deviations of about 4 % compared to 2D DIC measurements on ROI 2, as reported in Table 1.

Non-contact measurement techniques, such as virtual extensometers, allow measuring the relative displacement between two points on the specimen without introducing contact forces. Hence, they can provide similar information to physical extensometers, but avoiding the risk of influencing the deformation behaviour through physical contact. Moreover, the measurement can be taken at points less susceptible to the spurious bending effects, such as the specimen axis, avoiding the need for pair measurements and averaging.

If a detailed analysis of strain localisation is required, then DIC methods represent a powerful technique. 1D DIC is relatively undemanding and has a lower computational cost compared to full-field 2D tracking, as it processes data from a single line rather than the entire specimen surface. Despite its simplicity, it captures the strain localisation associated with the propagation of the martensitic transformation front, providing an effective visual representation of the phenomenon over time, as shown in Figure 4. However, for a comprehensive analysis of the deformation field, allowing the identification of the band deformation patterns as well as other localised deformation phenomena, 2D DIC comes as a more suitable solution. 2D DIC, performed on a ROI covering the whole specimen width, provides a full-field monitoring of the transformation fronts during the test (40).

Despite the additional computing steps, this allows detection of the regions of transformation nucleation (in the presented tests observed at the grips and at the extensometer knives) verifying the presence of weak zones and artefacts that could potentially invalidate the results. In fact, the deformation patterns observed in the presented tests reveal high sensitivity to inhomogeneities and significant influence from factors such as the specific specimen geometry, gripping conditions, the presence of extensometers, and the number of loading cycles. Hence, this type of full-field analysis is particularly useful for identifying potential sources of error, such as excessive bending or localised stress concentrations, which can significantly impact the material response. Material parameters calculated over an axial portion of the specimen distant from the grips (e.g., ROI 1) yield results very similar to those obtained from virtual extensometer and 1D DIC measurements over the same length, with an average deviation of 3 %, as shown in in Table 1.

Focusing the analysis on a smaller square ROI covering 25 % of the specimen width (ROI 2) allowed for a more accurate capture of the bipolar strain behaviour of nitinol, which provides high degree of precision in the determination of the material parameters. This methodology could also be considered for applications on material exhibiting heterogeneous deformation localisation such as plastic deformation and necking.

The analysis was focused on few loading cycles of the material, as these are relevant for a number of critical applications, such as nitinol cardiovascular implants. These normally undergo complete superelastic transformation only when collapsed in the delivery system and, once implanted, typically operate under small strains in the austenitic configuration. This necessarily implies that some of the observed changes may be related not just with the analysed measurement methods but also with the inherent material instability under cyclic loading. For other applications where fatigue is associated with cyclic phase changes, it might be appropriate to analyse the material parameters after pre-conditioning.

Ultimately, the choice of the measurement technique should be guided by the specific research objectives and the desired level of detail, also considering combinations of techniques, including full-field and localised measurements. All techniques demonstrated capable to provide reasonable estimates of plateau stresses, with the crosshead measurement suffering from larger approximation. However, while techniques like crosshead displacement can provide a simple estimate of overall strain, more advanced methods, such as virtual extensometers and DIC, are necessary for capturing the complex strain distributions associated with the phase transformation in nitinol.

5. Conclusion

This work presents a critical analysis of the most common strain measurement methodologies applied in quasi-static mechanical characterisation of nitinol. The study investigates the main advantages and disadvantages of each approach, including crosshead position, physical extensometers, virtual optical extensometers, 1D DIC and 2D DIC.

The results indicate that crosshead displacement provides a simplified representation of the actual strain behaviour. While physical extensometers provide higher accuracy in the determination of the main mechanical parameters, their reading is limited by the distance between the knives and depends on their specific location. To address this limitation, couples of extensometers arrangements are required. Moreover, they introduce spurious lateral forces at the knives locations resulting in localised compressions which can alter the material response. For this reason, the crosshead strain measurement is often favoured over the extensometer measurement, particularly for slender specimens like long wires. Non-contact techniques, such as virtual extensometers, offer a promising alternative by measuring strain without introducing contact forces. DIC analysis provides a comprehensive overview of the deformation field, enabling the identification of transformation front nucleation and propagation, as well as other localised deformation phenomena. It also allows focusing on lines or on small regions where the determination of the material parameters becomes more accurate.

In general, the optimal strain measurement technique depends on the specific research objectives and the desired level of detail. While all methods result suitable for the estimation of the overall mechanical parameters, with different degrees of accuracy, full-field DIC approaches are particularly suitable to capture the intricate strain distributions associated with nitinol phase transformation.

Funding

This work was supported by PON R&I 2014/2020, D.M. N. 1061 of 10 AGOSTO 2021.

Data availability

Data will be made available on request.

References

1. Wadood A. Brief overview on nitinol as biomaterial. Advances in Materials Science and Engineering. 2016;2016.
2. Liu Y, Xie Z, Humbeeck J Van, Delaey L, Liu Y. On the deformation of the twinned domain in NiTi shape memory alloys. Philosophical Magazine A: Physics of Condensed Matter, Structure, Defects and Mechanical Properties. 2000;80(8):1935–53.

3. Frost M, Sedlák P, Sedmák P, Heller L, Šittner P. SMA Constitutive Modeling Backed Up by 3D-XRD Experiments: Transformation Front in Stretched NiTi Wire. Shape Memory and Superelasticity. 2018;4(4):411–6.

4. Shaw JA, Kyriakides S. On the nucleation and propagation of phase transformation fronts in a NiTi alloy. Acta Mater. 1997;45(2):683–700.

5. Schlosser P, Favier D, Louche H, Orgéas L. Experimental characterization of NiTi SMAs thermomechanical behaviour using temperature and strain full-field measurements. CIMTEC 2008 - Proceedings of the 3rd International Conference on Smart Materials, Structures and Systems - State-of-the-art Research and Application of SMAs Technologies. 2008;59:140–9.

6. Zheng L, He Y, Moumni Z. Effects of Lüders-like bands on NiTi fatigue behaviors. Int J Solids Struct. 2016;83:28–44.

7. Shariat BS, Li Y, Yang H, Wang Y, Liu Y. Shear strain evolution during tension-induced Lüders-type deformation of polycrystalline NiTi plates. Materials Science and Engineering A [Internet]. 2022;839(January):142774. Available from: https://doi.org/10.1016/j.msea.2022.142774

8. Brinson LC, Schmidt I, Lammering R. Stress-induced transformation behavior of a polycrystalline NiTi shape memory alloy: Micro and macromechanical investigations via in situ optical microscopy. J Mech Phys Solids. 2004;52(7):1549–71.

9. Machado LG, Lagoudas DC. Modeling of SMAs. 2008.

10. Murasawa G, Kitamura K, Yoneyama S, Miyazaki S, Miyata K, Nishioka A, et al. Macroscopic stress-strain curve, local strain band behavior and the texture of NiTi thin sheets. Smart Mater Struct. 2009;18(5).

11. Senol K, Cao H, Tripathy S. Characterization and Validation of Fatigue Strains for Superelastic Nitinol Using Digital Image Correlation. J Med Device [Internet]. 2021 Dec 1;15(4). Available from: https://asmedigitalcollection.asme.org/medicaldevices/article/15/4/041005/1115578/Characterization-and-Validation-of-Fatigue-Strains

12. Zheng L, He Y, Moumni Z. Effects of Lüders-like bands on NiTi fatigue behaviors. Int J Solids Struct. 2016;83:28–44.

13. Bewerse C, Gall KR, McFarland GJ, Zhu P, Brinson LC. Local and global strains and strain ratios in shape memory alloys using digital imagecorrelation. Materials Science and Engineering: A [Internet]. 2013;568:134–42. Available from: http://dx.doi.org/10.1016/j.msea.2013.01.030

14. Daly S, Ravichandran G, Bhattacharya K. Stress-induced martensitic phase transformation in thin sheets of Nitinol. Acta Mater. 2007;55(10):3593–600.

15. Tsimpoukis S, Kyriakides S. Rate induced thermomechanical interactions in NiTi tensile tests on strips. J Mech Phys Solids [Internet]. 2024;184(December 2023):105530. Available from: https://doi.org/10.1016/j.jmps.2023.105530

16. Xiao R, Hou B, Sun QP, Zhao H, Li YL. An experimental investigation of the nucleation and the propagation of NiTi martensitic transformation front under impact loading. Int J Impact Eng. 2020;140(October 2019).

17. Xie X, Kan Q, Kang G, Lu F, Chen K. Observation on rate-dependent cyclic transformation domain of super-elastic NiTi shape memory alloy. Materials Science and Engineering: A [Internet]. 2016;671:32–47. Available from: http://dx.doi.org/10.1016/j.msea.2016.06.045

18. Zhang X, Feng P, He Y, Yu T, Sun Q. Experimental study on rate dependence of macroscopic domain and stress hysteresis in NiTi shape memory alloy strips. Int J Mech Sci [Internet]. 2010 Dec;52(12):1660–70. Available from: http://dx.doi.org/10.1016/j.ijmecsci.2010.08.007

19. Zhang Y, Chai X, Ju X, You Y, Zhang S, Zheng L, et al. Concentration of transformation-induced plasticity in pseudoelastic NiTi shape memory alloys: Insight from austenite-martensite interface instability. Int J Plast. 2023;160(July 2022):103481.

20. Xiao Y, Zeng P, Lei L, Du H. Local Mechanical Response of Superelastic NiTi Shape-Memory Alloy Under Uniaxial Loading. Shape Memory and Superelasticity. 2015;1(4):468–78.

21. Xiao Y, Zeng P, Lei L, Zhang Y. In situ observation on temperature dependence of martensitic transformation and plastic deformation in superelastic NiTi shape memory alloy. Mater Des [Internet]. 2017;134:111–20. Available from: https://doi.org/10.1016/j.matdes.2017.08.037

22. Kim K, Daly S. Experimental studies of phase transformation in shape memory alloys. Conference Proceedings of the Society for Experimental Mechanics Series. 2012;4:267–9.

23. Murasawa G, Yoneyama S, Sakuma T, Takashi M. Influence of cyclic loading on inhomogeneous deformation behavior arising in NiTi shape memory alloy plate. Mater Trans. 2006;47(3):780–6.

24. Bustos I, Soul H, Alonso G, Bertolino G, Yawny A. Heat Source Reconstruction and Its Relationship with Functional Fatigue of Pseudoelastic NiTi Ribbons. Shape Memory and Superelasticity. 2022;

25. Reedlunn B, Daly S, Hector L, Zavattieri P, Shaw J. Tips and tricks for characterizing shape memory wire part 5: Full-field strain measurement by digital image correlation. Exp Tech. 2013;37(3):62–78.

26. Xie X, Kan Q, Kang G, Li J, Qiu B, Yu C. Observation on the transformation domains of super-elastic NiTi shape memory alloy and their evolutions during cyclic loading. Smart Mater Struct [Internet]. 2016;25(4):0. Available from: http://dx.doi.org/10.1088/0964-1726/25/4/045003

27. Xiao Y, Jiang D. Effects of structural geometry on the localized deformation of superelastic NiTi sheets. Int J Solids Struct [Internet]. 2022;257(January):111762. Available from: https://doi.org/10.1016/j.ijsolstr.2022.111762

28. Petrini L, Migliavacca F. Biomedical Applications of Shape Memory Alloys. Journal of Metallurgy. 2011;2011(Figure 1):1–15.

29. Bozkurt S, Preston-Maher GL, Torii R, Burriesci G. Design, Analysis and Testing of a Novel Mitral Valve for Transcatheter Implantation. Ann Biomed Eng. 2017 Aug 3;45(8):1852–64.

30. ASTM E8. ASTM E8/E8M standard test methods for tension testing of metallic materials 1. Annual Book of ASTM Standards 4. 2010;(C):1–27.

31. ASTM F2516-14. ASTM F2516−14: Standard Test Method for Tension Testing of Nickel-Titanium Superelastic Materials. 2015.

32. Shaw JA, Kyriakides S. Thermomechanical aspects of NiTi. J Mech Phys Solids. 1995;43(8):1243–81.

33. Orgéas L, Favier D. Stress-induced martensitic transformation of a NiTi alloy in isothermal shear, tension and compression. Acta Mater. 1998;46(15):5579–91.

34. Prabhakaran R, Galloway TL. Strain measurement in a shape memory alloy with strain gauges. Strain. 2005;41(4):177–84.

35. Delpueyo D, Jury A, Balandraud X, Grédiac M. Applying Full-Field Measurement Techniques for the Thermomechanical Characterization of Shape Memory Alloys: A Review and Classification. Shape Memory and Superelasticity [Internet]. 2021 Dec 10;7(4):462–90. Available from: https://link.springer.com/10.1007/s40830-021-00355-w

36. Kim K, Daly S. Martensite Strain Memory in the Shape Memory Alloy Nickel-Titanium Under Mechanical Cycling. Exp Mech. 2011;51(4):641–52.

37. Zhang S, He Y. Fatigue resistance of branching phase-transformation fronts in pseudoelastic NiTi polycrystalline strips. Int J Solids Struct [Internet]. 2018;135:233–44. Available from: https://doi.org/10.1016/j.ijsolstr.2017.11.023

38. Catoor D, Ma Z, Kumar S. Cyclic response and fatigue failure of Nitinol under tension–tension loading. J Mater Res. 2019;34(20):3504–22.

39. Jiang D, Kyriakides S, Landis CM, Kazinakis K. Modeling of propagation of phase transformation fronts in NiTi under uniaxial tension. European Journal of Mechanics, A/Solids [Internet]. 2017;64:131–42. Available from: http://dx.doi.org/10.1016/j.euromechsol.2017.02.004

40. Di Leonardo S, Pitarresi G, Burriesci G. Standard mechanical testing is inadequate for the mechanical characterisation of shape-memory alloys: Source of errors and a new corrective approach. Mater Des [Internet]. 2022;216:110538. Available from: https://doi.org/10.1016/j.matdes.2022.110538

41. Bian X, Saleh AA, Pereloma E V, Davies CHJ, Gazder AA. A digital image correlation study of a NiTi alloy subjected to monotonic uniaxial and cyclic loading-unloading in tension. Materials Science and Engineering: A [Internet]. 2018 May;726(April):102–12. Available from: https://doi.org/10.1016/j.msea.2018.04.081

42. Ahadi A, Sarvari E, Frenzel J, Eggeler G. Journal of the Mechanics and Physics of Solids Size-dependent transformation patterns in NiTi tubes under tension and bending : Stereo digital image correlation experiments and modeling. 2026;206(June 2025).

43. Pinto V, Cappello R, Di Leonardo S, Catalanotti G, Burriesci G, Pitarresi G. Evaluation of NiTi under low-amplitude cyclic loading by means of thermographic harmonic analysis. Mechanics of Materials. 2025;206(March).

44. Zheng L, He Y, Moumni Z. Investigation on fatigue behaviors of NiTi polycrystalline strips under stress-controlled tension via in-situ macro-band observation. Int J Plast [Internet]. 2017;90:116–45. Available from: http://dx.doi.org/10.1016/j.ijplas.2016.12.008

45. Wang Z, Luo J, Kuang W, Jin M, Liu G, Jin X, et al. Strain Rate Effect on the Thermomechanical Behavior of NiTi Shape Memory Alloys: A Literature Review. Metals (Basel). 2023;13(1).

46. ASTM F2004-03. ASTM F2004-03 Transformation Temperature of Nickel-Titanium Alloys by Thermal Analysis 1. ASTM International. 2018;05(Reapproved 2010):11–4.

47. Bustos I, Soul H, Alonso G, Bertolino G, Yawny A. Heat Source Reconstruction and Its Relationship with Functional Fatigue of Pseudoelastic NiTi Ribbons. Shape Memory and Superelasticity. 2022;

48. Elibol C, Wagner MFX. Virtual extensometer analysis of martensite band nucleation, growth, and strain softening in pseudoelastic NiTi subjected to different load cases. Materials. 2018;11(8).

49. Pan B, Qian K, Xie H, Asundi A. Two-dimensional digital image correlation for in-plane displacement and strain measurement : a review. 2009;062001.

50. Blaber J, Adair B, Antoniou A. Ncorr: Open-Source 2D Digital Image Correlation Matlab Software. Exp Mech. 2015;55(6):1105–22.

51. Pan B. Recent Progress in Digital Image Correlation. Exp Mech. 2011;51(7):1223–35.

52. Reedlunn B, Churchill CB, Nelson EE, Shaw JA, Daly SH. Tension, compression, and bending of superelastic shape memory alloy tubes. J Mech Phys Solids. 2014;63(1):506–37.